

## QUASARS PROBING QUASARS IX. THE KINEMATICS OF THE CIRCUMGALACTIC MEDIUM SURROUNDING $Z \sim 2$ QUASARS

MARIE WINGYEE LAU<sup>1,2</sup>, J. XAVIER PROCHASKA<sup>2</sup>, JOSEPH F. HENNAWI<sup>3</sup>

*Draft version March 23, 2018*

### ABSTRACT

We examine the kinematics of the gas in the environments of galaxies hosting quasars at  $z \sim 2$ . We employ 148 projected quasar pairs to study the circumgalactic gas of the foreground quasars in absorption. The sample selects foreground quasars with precise redshift measurements, using emission-lines with precision  $\lesssim 300 \text{ km s}^{-1}$  and average offsets from the systemic redshift  $\lesssim |100 \text{ km s}^{-1}|$ . We stack the background quasar spectra at the foreground quasar's systemic redshift to study the mean absorption in C II, C IV, and Mg II. We find that the mean absorptions exhibit large velocity widths  $\sigma_v \approx 300 \text{ km s}^{-1}$ . Further, the mean absorptions appear to be asymmetric about the systemic redshifts. The mean absorption centroids exhibit small redshift relative to the systemic  $\delta v \approx +200 \text{ km s}^{-1}$ , with large intrinsic scatter in the centroid velocities of the individual absorption systems. We find the observed widths are consistent with gas in gravitational motion and Hubble flow. However, while the observation of large widths alone does not require galactic-scale outflows, the observed offsets suggest that the gas is on average outflowing from the galaxy. The observed offsets also suggest that the ionizing radiation from the foreground quasars is anisotropic and/or intermittent.

*Keywords:* galaxies: clusters: intracluster medium – galaxies: formation – galaxies: halos – intergalactic medium – quasars: absorption lines – quasars: general

### 1. INTRODUCTION

Galaxy formation and evolution are driven by the flows of gas into and out of their interstellar medium. Current theories demand that star-forming galaxies maintain these flows. Gas accretes, cools, and adds to the fuel supply, while star formation feedback heats gas, blows it out of galaxies, and regulates star formation (for a review see Somerville & Davé 2015).

Direct observations of galactic flows are difficult to acquire. Detecting the presence of the gas is itself challenging. Either the gas mass is too small, or the gas density is too low for the detection of line-emission, e.g. 21 cm, Ly $\alpha$ , or H $\alpha$  from H I. Resolving the kinematics and establishing the mass flux pose an even greater challenge. These challenges are accentuated for distant, young galaxies, where flows of gas are predicted to prevail (Kereš et al. 2009; Fumagalli et al. 2011). Therefore, with rare exceptions, (e.g., Cantalupo et al. 2014; Hennawi et al. 2015), the community has relied on absorption-line spectroscopy to detect and characterize the gas surrounding galaxies (e.g., Bergeron & Boisse 1991; Steidel et al. 2010; Prochaska et al. 2011; Tumlinson et al. 2013). In a previous paper of the Quasars Probing Quasars series (Lau et al. 2016, hereafter QPQ8), we measured the velocity field for C II 1334 and C IV 1548, finding that the circumgalactic medium frequently exhibits large velocity widths that are offset from the systemic redshift. From a sample of 7 C II systems and 10 C IV systems, we measured the velocity interval that encompasses 90% of the total optical depth,  $\Delta v_{90}$ , and the  $1\sigma$  dispersion relative to

the profile centroid,  $\sigma_v$ . The median  $\Delta v_{90}$  is  $555 \text{ km s}^{-1}$  for C II 1334 and is  $342 \text{ km s}^{-1}$  for C IV 1548. The median  $\sigma_v$  is  $249 \text{ km s}^{-1}$  for C II 1334 and is  $495 \text{ km s}^{-1}$  for C IV 1548. These velocity fields exceed all previous measurements from galaxies and/or absorption systems at any epoch. The offsets,  $\delta v$ , are often positive, with the sign convention that positive velocities indicate a redshift from the systemic.

With absorption-line spectroscopy of background sightlines, other researchers also have had success in characterizing the flows of gas around galaxies. Rakic et al. (2012) found a net large-scale inflow around star-forming galaxies, or a Kaiser effect for gas on 1–2 Mpc scales. Ho et al. (2017) found gas spiraling inward near the disk plane of star-forming galaxies on  $< 100 \text{ kpc}$  scales. Johnson et al. (2015) studied the CGM surrounding  $z \sim 1$  quasars. They found large peculiar motions in the gas exceeding the expected virial velocity, with quasar-driven outflows being one possible explanation. However, we consider that their velocity spreads can be better quantified. Other existing studies that found large velocity spreads are single sightlines (e.g., Tripp et al. 2011; Rudie et al. 2017), or with gas tracing a higher ionization state than the QPQ absorption systems (e.g., Churchill et al. 2012), or where the average velocity spread is smaller than that measured in QPQ8. In Gauthier (2013), where a single sightline is reported, the  $\Delta v_{90}$  of the Mg II absorption is less than the average of the QPQ8 C II absorption. In Muzahid et al. (2015), an absorber is found with  $\Delta v_{90}$  smaller than  $555 \text{ km s}^{-1}$  in O VI and N V, and still smaller for other ions. The Zahedy et al. (2016) sample likewise has average  $\Delta v_{90}$  smaller than that of QPQ8.

A significant limitation of absorption-line analysis of transverse sightlines, especially regarding galactic-scale flows, is the inherent symmetry of the experiment. One

<sup>1</sup> Email: lwymarie@ucolick.org

<sup>2</sup> Department of Astronomy and Astrophysics, UCO/Lick Observatory, University of California, 1156 High Street, Santa Cruz, CA 95064

<sup>3</sup> Department of Physics, Broida Hall, University of California, Santa Barbara, CA 93106-9530

generally lacks any constraint on the distance of the gas along the sightline. Positive or negative velocities with respect to the galaxy may be interpreted as gas flowing either toward or away from the system. “Down-the-barrel” observations break this symmetry, and have generally provided evidence for flows away from galaxies (Rupke et al. 2005; Martin 2005; Weiner et al. 2009; Rubin et al. 2014). However, these data are frequently at low spectral resolution which limits one’s sensitivity to inflowing gas.

In this paper (hereafter QPQ9), we examine the flows of gas in the environments of massive galaxies hosting quasars. Our approach leverages a large dataset of quasar pairs (Hennawi et al. 2006, hereafter QPQ1) to use the standard techniques of absorption-line spectroscopy with background quasars. These quasar pairs have angular separations that correspond to less than 300 kpc projected separation at the foreground quasar’s redshift. Our previous publications from these quasar pairs have established that these galaxies are surrounded by a massive, cool, and enriched CGM (QPQ5, QPQ6, QPQ7: Prochaska et al. 2013b,a, 2014). We have collected a sample of 148 background spectra that are paired with foreground quasars with precisely measured redshifts. Among the sightlines in the QPQ9 sample, 13 have spectral resolution  $R > 5000$  from echellette or echelle observations, and have been analyzed separately in QPQ8 (see their Figure 8, 9, and 10, and their Appendix). In QPQ8, where the individual metal-bearing absorption components are resolved, 15 out of the 21 components are at positive velocities relative to the sys-

temic redshift. For this current work, we stack spectra of all resolutions instead of performing a component-by-component analysis. Our primary scientific interests are twofold: (i) search for signatures of galactic-scale outflows from the central galaxy, presumably driven by recent star formation and/or active galactic nuclei feedback; (ii) characterize the dynamics of the gas around these massive systems. We further describe an aspect of this experiment that offers a unique opportunity to study galactic-scale flows: we argue that, the anisotropic or intermittent radiation from the foreground quasars may break the symmetry in the velocity field of circumgalactic absorbers. If the ionizing radiation field is asymmetric, the absorbers may also distribute asymmetrically. Alternatively, finite quasar lifetime will result in different radiation fields impinged on the gas closer to versus further away from the background quasar, due to different light travel times. Kirkman & Tytler (2008) reported an asymmetry in H I absorption on scales larger than the CGM, and gave similar arguments on anisotropy or intermittence.

We adopt a  $\Lambda$ CDM cosmology with  $\Omega_M = 0.26$ ,  $\Omega_\Lambda = 0.74$ , and  $H_0 = 70 \text{ km s}^{-1} \text{ Mpc}^{-1}$ . Distances are proper unless otherwise stated. When referring to comoving distances we include explicitly an  $h^{-1}$  term and follow modern convention of scaling to the Hubble constant  $h = H_0/(70 \text{ km s}^{-1} \text{ Mpc}^{-1})$ .

## 2. THE EXPERIMENT

**Table 1**  
Properties of the Projected Quasar Pairs in the QPQ9 sample

Foreground Quasar	$z_{\text{fg}}$	Line for $z_{\text{fg}}^a$	Background Quasar	$z_{\text{bg}}$	BG Quasar Instrument	$R_\perp$ (kpc)	$g_{\text{UV}}$
J003423.05–1050020	1.8388	MgII	J003423.44-104956.3	1.948	LRIS	67	11938
J004220.66+003218.7	1.9259	MgII	J004218.72+003237.1	3.048	BOSS	299	97
J004745.49+310120.3	1.9706	MgII	J004745.61+310138.3	2.695	BOSS	157	1723
J004757.26+144741.0	1.6191	MgII	J004757.88+144744.7	2.757	BOSS	82	6697
J005717.36–000113.3	2.1611	[OIII]	J005718.99-000134.7	2.511	BOSS	271	1283
J010323.84–000254.2	1.7506	MgII	J010324.37-000251.3	2.306	BOSS	74	5462
J014328.77+295436.8	1.8007	MgII	J014330.89+295439.9	2.018	BOSS	243	997
J014917.11–002141.6	1.6834	MgII	J014917.46-002158.5	2.159	SDSS	155	2390
J021416.96–005229.1	1.8002	MgII	J021416.12-005251.5	2.332	BOSS	225	564
J022447.89–004700.4	1.6959	MgII	J022448.85-004638.9	2.188	BOSS	226	293
J023018.27–033319.4	2.3817	MgII	J023019.99-033315.0	2.985	BOSS	221	1444
J023315.44–000303.6	1.7205	MgII	J023315.75-000231.4	1.839	BOSS	286	101
J023946.43–010640.4	2.299	[OIII]	J023946.45-010644.1	3.124	BOSS	32	20931
J024603.68–003211.8	1.603	MgII	J024602.35-003221.6	2.153	BOSS	195	1889
J025038.68–004739.2	1.8538	MgII	J025039.82-004749.6	2.445	BOSS	175	4007
J034138.16+000002.9	2.1246	MgII	J034139.19-000012.7	2.243	GMOS-N	190	392
J040955.87–041126.9	1.7166	MgII	J040954.21-041137.1	2.0	SDSS	235	715
J072739.55+392855.3	1.9853	MgII	J072739.72+392919.5	2.433	BOSS	210	403
J075009.25+272405.2	1.7713	MgII	J075008.27+272404.5	1.802	LRIS	114	1370
J075259.81+401128.2	1.8844	MgII	J075259.14+401118.2	2.121	SDSS	110	1060
J080049.89+354249.6	1.9825	[OIII]	J080048.74+354231.3	2.066	LRIS	201	2074
J080537.29+472339.3	1.8913	MgII	J080538.78+472404.8	2.964	BOSS	259	367
J080945.17+453918.1	2.0392	MgII	J080948.22+453929.0	2.278	BOSS	292	195
J081223.17+262000.9	1.6427	MgII	J081223.89+262012.5	2.17	BOSS	132	3442
J081419.58+325018.7	2.1744	[OIII]	J081420.38+325016.1	2.213	GMOS-N	90	2899
J081832.87+123219.9	1.7032	MgII	J081833.97+123215.4	2.234	BOSS	147	6609
J082346.05+532527.8	1.6467	MgII	J082347.49+532519.1	1.86	BOSS	136	820
J082421.01+531249.3	2.0855	MgII	J082420.02+531315.2	2.165	BOSS	237	340
J082843.37+454517.3	1.873	MgII	J082844.87+454518.2	1.987	LRIS	137	525
J083030.38+545228.8	1.6702	MgII	J083029.11+545210.3	3.337	BOSS	188	1506
J083713.56+363037.3	1.8364	MgII	J083712.69+363037.7	2.301	MODS1	92	5012
J083757.91+383727.1	2.0624	H $\alpha$	J083757.13+383722.4	2.251	LRIS	89	8609
J083854.52+462124.4	1.7596	MgII	J083852.94+462137.6	2.163	BOSS	184	673
J084158.47+392120.0	2.0414	[OIII]	J084159.26+392139.0	2.214	LRIS	183	1514
J084511.89+464135.5	1.6295	MgII	J084509.64+464113.0	1.898	BOSS	283	135

Table 1 — *Continued*

Foreground Quasar	$z_{\text{fg}}$	Line for $z_{\text{fg}}^a$	Background Quasar	$z_{\text{bg}}$	BG Quasar Instrument	$R_{\perp}$ (kpc)	$g_{UV}$
J085019.43+475538.5	1.8164	MgII	J085021.17+475516.0	1.891	BOSS	249	392
J085151.38+522901.6	1.9738	MgII	J085154.53+522910.6	2.031	BOSS	262	265
J085249.45+471423.1	1.6468	MgII	J085248.55+471419.3	1.688	BOSS	87	7078
J085358.36-001108.0	2.4016	[OIII]	J085357.49-001106.2	2.579	MagE	112	1231
J085629.48+551450.2	1.6228	MgII	J085630.45+551417.5	1.932	BOSS	296	466
J085737.58+390120.5	1.9529	MgII	J085738.00+390136.0	2.848	BOSS	150	1984
J090417.94+004148.2	1.6193	MgII	J090419.12+004205.1	1.645	SDSS	214	1035
J090657.78+100121.4	1.6965	MgII	J090657.62+100105.6	2.525	BOSS	141	6960
J091046.44+041458.5	2.0461	[OIII]	J091046.69+041448.4	2.377	MagE	95	11897
J091217.57+413933.5	1.7764	MgII	J091215.75+413948.2	2.198	BOSS	220	790
J091234.27+305616.2	1.6237	MgII	J091236.32+305626.5	2.146	BOSS	247	514
J091338.33-010708.7	2.7491	MgII	J091338.97-010704.6	2.916	XSHOOTER	89	5830
J091432.02+010912.4	2.1404	[OIII]	J091430.85+010927.5	2.475	BOSS	199	1222
J091551.72+011900.2	1.9706	MgII	J091553.37+011911.4	2.102	BOSS	236	970
J092405.06+474611.4	2.0556	MgII	J092402.85+474600.7	2.098	BOSS	214	341
J092417.65+392920.3	1.8864	MgII	J092416.72+392914.6	2.08	LRIS	106	2788
J092543.88+372504.9	2.0704	MgII	J092544.71+372503.5	2.314	BOSS	94	3890
J093226.34+092526.1	2.4172	[OIII]	J093225.66+092500.2	2.602	MagE	238	774
J093317.43+592027.4	1.8617	MgII	J093320.57+592036.5	2.633	BOSS	224	1441
J093640.35-005840.1	2.2098	MgII	J093642.12-005831.3	2.731	BOSS	250	496
J093936.83+482115.0	1.8878	MgII	J093938.97+482059.4	2.415	BOSS	230	528
J093952.56+505207.4	1.6105	MgII	J093954.75+505148.8	2.476	BOSS	242	128
J094133.64+230840.1	1.7762	MgII	J094135.61+230845.8	2.551	BOSS	243	1700
J094906.23+465938.4	1.7204	MgII	J094906.52+465909.6	2.173	BOSS	253	243
J095127.06+493248.3	1.7407	MgII	J095126.22+493218.8	1.83	BOSS	268	293
J095858.88+491253.1	2.0505	MgII	J095858.06+491307.5	2.155	BOSS	144	722
J100046.45+033708.8	1.7006	MgII	J100048.52+033708.8	2.353	BOSS	271	255
J100509.56+501929.8	1.8176	MgII	J100507.07+501929.8	2.019	LRIS	211	330
J100627.47+480420.0	2.3034	[OIII]	J100627.11+480429.9	2.597	BOSS	90	2886
J100913.91+023612.4	1.7359	MgII	J100913.33+023643.0	2.216	BOSS	287	342
J100941.35+250104.1	1.8703	MgII	J100940.58+250053.9	1.981	LRIS	127	3588
J101001.51+403755.5	2.1924	H $\alpha$	J101003.47+403754.9	2.505	BOSS	191	5421
J101323.89+033016.0	1.9401	MgII	J101322.23+033009.1	2.273	BOSS	219	426
J101753.38+622653.4	1.6528	MgII	J101750.44+622648.2	2.738	BOSS	184	922
J101947.11+494835.8	1.6224	MgII	J101947.0+494835.1	1.652	LRIS	117	881
J102007.23+611955.0	1.7909	MgII	J102010.05+611950.3	2.387	BOSS	180	1817
J102259.33+491125.8	1.9757	MgII	J102259.97+491151.7	2.469	BOSS	231	212
J102821.26+240121.8	1.8709	MgII	J102822.18+240057.4	2.414	BOSS	240	834
J103443.62+085702.0	1.6395	MgII	J103442.26+085645.7	2.766	BOSS	233	700
J103628.12+501157.9	2.0097	MgII	J103630.52+501219.8	2.228	BOSS	271	1198
J103857.37+502707.0	3.1325	[OIII]	J103900.01+502652.8	3.236	ESI	233	3567
J103946.92+454716.0	1.8644	MgII	J103945.58+454707.4	2.456	BOSS	148	675
J104244.84+650002.7	1.9876	MgII	J104245.14+645936.7	2.124	BOSS	227	703
J104435.62+313950.7	1.7062	MgII	J104434.76+313957.7	2.377	BOSS	115	1873
J104955.01+231358.2	1.8439	MgII	J104953.97+231401.3	2.171	BOSS	129	1813
J105221.77+555253.5	1.9989	MgII	J105218.36+555311.3	2.278	BOSS	293	846
J105246.45+641832.2	1.6429	MgII	J105251.42+641838.5	2.936	BOSS	286	127
J111339.86+330604.8	1.8913	MgII	J111337.84+330553.3	2.413	BOSS	243	853
J111850.44+402553.8	1.9257	MgII	J111851.45+402557.6	2.317	BOSS	106	1946
J112858.89+644440.4	1.6561	MgII	J112854.14+644427.4	2.217	BOSS	289	149
J113852.65+632934.0	1.8855	MgII	J113851.73+632955.6	2.625	BOSS	196	1912
J114435.54+095921.7	2.9734	[OIII]	J114436.65+095904.9	3.16	MIKE-Red	189	2914
J114439.51+454115.8	1.687	MgII	J114442.48+454111.3	2.592	BOSS	275	78
J114546.54+032236.7	1.7664	MgII	J114546.22+032251.9	2.011	MagE	139	779
J115253.09+150706.5	1.7883	MgII	J115254.97+150707.8	3.349	BOSS	237	622
J115457.16+471149.3	1.6819	MgII	J115458.69+471209.9	1.947	SDSS	226	60
J115502.45+213235.5	1.9551	MgII	J115504.25+213254.0	2.695	BOSS	277	397
J115529.49+463413.1	1.6491	MgII	J115528.75+463442.9	2.329	BOSS	270	326
J115533.62+393359.2	1.6118	MgII	J115531.32+393415.4	2.555	BOSS	272	742
J120224.68+074800.3	1.6613	MgII	J120226.48+074739.7	2.767	BOSS	296	584
J120417.47+022104.7	2.436	[OIII]	J120416.69+022110.0	2.532	HIRES	112	2710
J120856.94+073741.2	2.1708	MgII	J120857.16+073727.3	2.616	MagE	123	3853
J121159.88+324009.0	1.978	MgII	J121201.69+324013.3	2.273	BOSS	209	1046
J121344.28+471958.7	1.8371	MgII	J121343.01+471931.0	3.275	BOSS	260	491
J1215590+571616.6	1.93	[OIII]	J121558.82+571555.5	1.964	BOSS	184	614
J121657.82+152706.6	1.9473	MgII	J121657.00+152712.7	2.318	BOSS	116	4225
J122514.29+570942.3	1.8953	MgII	J122517.89+570943.7	2.224	BOSS	255	330
J123143.01+002846.3	3.2015	[OIII]	J123141.73+002913.9	3.308	GMOS-S	271	1490
J124632.33+234531.2	1.9937	MgII	J124632.19+234509.5	2.573	BOSS	188	1886
J124846.05+405758.2	1.8265	MgII	J124846.97+405820.9	2.463	BOSS	219	897
J130124.74+475909.6	2.194	H $\alpha$	J130125.67+475930.8	2.765	SDSS	199	4932
J130605.19+615823.7	2.1089	H $\alpha$	J130603.55+615835.2	2.175	LRIS	141	1761
J130714.79+463536.6	1.6226	MgII	J130716.07+463511.2	2.248	BOSS	251	137
J131341.32+454654.6	1.6878	MgII	J131342.78+454658.2	2.241	BOSS	139	1098
J132514.97+540930.6	2.0507	MgII	J132511.07+540927.0	3.235	BOSS	298	514
J133026.12+411432.0	2.0645	MgII	J133023.67+411445.9	2.217	BOSS	271	384

Table 1 — *Continued*

Foreground Quasar	$z_{\text{fg}}$	Line for $z_{\text{fg}}^a$	Background Quasar	$z_{\text{bg}}$	BG Quasar Instrument	$R_{\perp}$ (kpc)	$g_{UV}$
J133924.02+462808.2	1.8539	MgII	J133922.31+462749.2	3.391	BOSS	226	940
J134650.08+195235.2	2.0697	MgII	J134648.19+195253.1	2.523	BOSS	278	884
J135306.35+113804.7	1.6315	MgII	J135307.90+113805.5	2.431	BOSS	213	8963
J135849.71+273806.9	1.9008	MgII	J135849.54+273756.9	2.127	LRIS	89	1765
J140208.01+470111.1	1.9161	[OIII]	J140209.52+470117.8	2.269	BOSS	140	1437
J140918.01+522552.4	1.8808	MgII	J140916.98+522535.3	2.109	SDSS	170	583
J141337.18+271517.1	1.6905	MgII	J141337.96+271511.0	1.965	BOSS	105	609
J142003.67+022726.7	3.617	[OIII]	J142004.12+022708.8	4.191	ESI	144	2291
J142054.42+160333.3	2.0221	[OIII]	J142054.92+160342.9	2.057	MagE	104	7811
J142215.57+465230.7	1.748	MgII	J142214.63+465254.6	2.338	BOSS	225	639
J142758.89-012130.4	2.2738	[OIII]	J142758.74-012136.2	2.354	MIKE	53	34208
J143109.67+572728.0	1.6802	MgII	J143109.22+572726.4	2.063	BOSS	39	5166
J143312.56+082651.8	1.8807	MgII	J143313.99+082714.0	2.432	BOSS	274	531
J143345.55+064109.0	2.294	[OIII]	J143344.55+064111.9	2.34	BOSS	122	1130
J143609.15+313426.7	1.8774	MgII	J143610.68+313418.9	2.562	BOSS	183	2188
J144211.25+530252.0	1.6461	MgII	J144209.98+530308.0	2.632	BOSS	179	439
J144232.92+013730.4	1.8079	MgII	J144231.91+013734.8	2.274	BOSS	137	1988
J144429.34+311321.2	1.7355	MgII	J144427.96+311313.0	1.795	LRIS	173	8820
J150814.06+363529.4	1.8493	MgII	J150812.78+363530.3	2.105	BOSS	133	5111
J153328.83+142542.5	2.0782	MgII	J153329.17+142537.8	2.564	BOSS	59	3898
J153456.02+215342.3	1.6712	MgII	J153455.85+215324.7	2.529	BOSS	156	1702
J153954.74+314629.3	1.8747	MgII	J153952.46+314625.2	2.235	BOSS	256	1080
J155325.61+192140.0	2.01	[OIII]	J155325.89+192137.7	2.098	MagE	44	5576
J155422.88+124438.0	1.8169	MgII	J155424.39+124431.5	2.394	BOSS	202	1349
J155947.73+494307.3	1.8615	MgII	J155946.28+494326.7	1.945	LRIS	210	1743
J160547.61+511330.5	1.783	MgII	J160546.67+511322.9	1.844	LRIS	102	4045
J161930.94+192620.9	1.7821	MgII	J161929.78+192645.4	2.39	BOSS	258	538
J162738.63+460538.4	3.8149	[OIII]	J162737.25+460609.3	4.11	ESI	253	1959
J163121.74+433317.3	2.0182	MgII	J163123.57+433317.3	2.631	BOSS	172	4090
J165442.21+251249.2	1.7207	MgII	J165444.38+251306.2	2.341	BOSS	298	459
J165716.85+310513.0	2.1331	MgII	J165716.52+310524.5	2.395	MODS1	98	5222
J214620.69-075250.6	2.1155	[OIII]	J214620.99-075303.8	2.577	MagE	120	4869
J214813.26+263059.4	1.6285	MgII	J214814.36+263129.7	3.286	BOSS	295	78
J220248.61+123645.5	2.0697	[OIII]	J220248.31+123656.3	2.512	BOSS	100	9466
J233845.19-000327.1	2.4399	[OIII]	J233845.45-000331.8	2.997	XSHOOTER	51	3674
J235505.22+320058.0	1.8159	MgII	J235505.33+320105.4	2.367	BOSS	56	2271
J235819.92+342455.8	1.6235	MgII	J235819.33+342506.5	2.02	BOSS	113	480

<sup>a</sup> The emission-line analyzed for measuring  $z_{\text{fg}}$ .

The goal of our experiment is to measure the average velocity fields of the absorption from  $\text{C}^+$ ,  $\text{C}^{3+}$ , and  $\text{Mg}^+$  ions associated with the CGM of the galaxies hosting  $z \sim 2$  quasars.

From our QPQ survey<sup>4</sup>, we analyze a subset of systems that pass within transverse separation  $R_{\perp} < 300$  kpc from a foreground quasar with  $z_{\text{fg}} > 1.6$ . We restrict the sample to foreground quasars with redshift measured from Mg II 2800, [O III] 5007, or  $\text{H}\alpha$  emission, giving a precision of  $300 \text{ km s}^{-1}$  or better and an average offset from the systemic redshift of  $|100 \text{ km s}^{-1}|$  or less. According to Shen et al. (2016a), the [O III] emission-line redshifts have the smallest scatter (intrinsic scatter and measurement error combined) of  $68 \text{ km s}^{-1}$  about the systemic redshift, and we analyze the sub-sample with [O III] redshifts separately. The [O III] line has an average blueshift of  $48 \text{ km s}^{-1}$  about the systemic redshift, which has been added when we compute the redshift of the line. The scatter and average offset of [O III] redshifts reported by Shen et al. (2016a) is consistent with the numbers reported by Boroson (2005) using a larger but lower redshift sample. Systemic redshifts measured from Mg II have a precision of  $226 \text{ km s}^{-1}$  according to Shen et al. (2016a), and we have taken into account their

reported median blueshift of  $57 \text{ km s}^{-1}$  of Mg II from the systemic. We note that Richards et al. (2002) reported a median redshift of  $97 \text{ km s}^{-1}$  of Mg II from [O III] using a larger but lower redshift sample. In QPQ8, we quantified the precision of  $\text{H}\alpha$  to be  $300 \text{ km s}^{-1}$  and the median offset from the systemic redshift is close to zero, consistent with the velocity shifts measured by Shen et al. (2011). Although  $\text{H}\beta$  is a narrow emission-line, we do not consider its redshift sufficiently reliable for use as systemic redshift.  $\text{H}\beta$  redshifts have a large scatter about the systemic  $\approx 400 \text{ km s}^{-1}$ , and a large average offset about the systemic  $\approx 100 \text{ km s}^{-1}$  (Shen et al. 2016a, QPQ8). Our line-centering algorithm calculates the mode of a line given by  $3 \times \text{median} - 2 \times \text{mean}$ , applied to the upper 60% of the emission, while Shen et al. (2016a) calculates the peak of a line. We expect that our line-centering algorithm gives emission redshifts very comparable to the Shen et al. (2016a) algorithm, however. Shen et al. (2016a) states that the difference between the peak and the centroid of an emission-line is not significant except for the broad line  $\text{H}\beta$ , which we do not use in redshift measurements. To quantify the above, we further obtain individual measurements of centroids and peaks in the Shen et al. (2016a) sample through private communication. We found there is essentially no difference between using the centroid versus using the peak for [O III] emission redshifts, and there is on average  $50 \text{ km s}^{-1}$  difference for Mg II. We may expect the difference between

<sup>4</sup> <http://www.qpqsurvey.org>

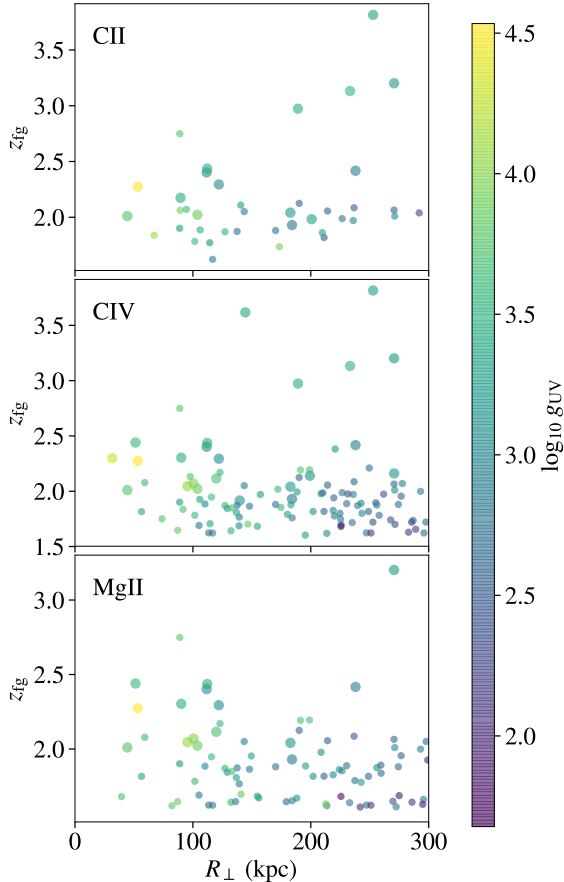


**Figure 1.** These panels summarize properties of the QPQ9 dataset. The QPQ survey selects quasar pairs of  $R_{\perp} < 300$  kpc and  $z_{fg} > 1.6$ . Assuming that the foreground quasars emit isotropically and at a distance equal to the impact parameter, the enhancement in the UV flux relative to the extragalactic UV background,  $g_{UV}$ , can be estimated. Large symbols correspond to foreground quasars with the most precise redshift measurement from [O III] 5007, while small symbols correspond to  $z_{fg}$  measurements from Mg II 2800, H $\alpha$ , or H $\beta$  emission. The top panel shows quasar pairs with coverage of C II 1334 at  $z_{fg}$  in the background quasar spectra. The middle panel shows pairs with coverage of C IV 1548. The bottom panel shows pairs with coverage of Mg II 2796.

the mode and the peak is even smaller. Hence, we argue that the average systemic bias corrections measured in Shen et al. (2016a) may be self-consistently applied to our measured emission-line redshifts to obtain systemic redshifts.

We further add to the QPQ dataset with quasar pairs selected from the public dataset of *igmspec*<sup>5</sup> (Prochaska 2017), which includes the spectra from the quasar catalogs based upon the Sloan Digital Sky Survey Seventh Data Release (Schneider et al. 2010) and the Twelfth Data Release (Pâris et al. 2017). We only select pairs with  $z_{fg}$  measurable using a robust Mg II 2800 emission-line. We reach a final sample size of 148. Figure 1 summarizes the experimental design. We refer the reader to previous QPQ publications for the details on the emission-line centering algorithm, data reduction, and continuum normalization (QPQ1; QPQ6; QPQ8).

As in the previous QPQ papers, we select the quasar pairs to have redshift difference  $> 3000$  km s<sup>-1</sup>, to ex-

clude physically associated binary quasars. The cut on velocity difference is motivated by the typical redshift uncertainty of  $\approx 500$  km s<sup>-1</sup> of the background quasars. In QPQ8, it was required that the observed wavelengths of the metal ion transitions fall outside the Ly $\alpha$  forest of the background quasar. In this paper, we exclude a small window around the Ly $\alpha$  emission, in addition to the Ly $\alpha$  forest, from analysis. For stacked profile analysis, a good estimate of the continuum level is necessary. In QPQ8 we found that absorption associated to the foreground quasar occurs within  $\pm 2000$  km s<sup>-1</sup> around  $z_{fg}$ . Therefore, it is desirable to keep a  $\approx \pm 3000$  km s<sup>-1</sup> window relatively free of contamination from Ly $\alpha$  forest. Taking into account the redshift uncertainties, we decide that at least one transition among C II 1334, C IV 1548, and Mg II 2796 at  $z_{fg}$  must lie redward of  $(1215.6701 + 20) \times (1 + z_{bg})$  Å, for a pair to be included in the analysis.

Furthermore, we include only those spectra with average signal-to-noise ratio (S/N) exceeding 5.5 per rest-frame Å in a  $\pm 3000$  km s<sup>-1</sup> window centered on the observed wavelengths of the metal ion transitions. This criterion is a compromise between maximizing sample size versus maintaining good data quality on the individual sightlines. We find that S/N  $> 5.5$  per rest-frame Å is necessary for properly estimating the continuum, as well as identifying mini-broad absorption line systems associated to the background quasar, which will significantly depress the flux level. We also require that the region of the spectrum that is  $\pm 3000$  km s<sup>-1</sup> around a considered metal ion transition does not overlap with strong atmospheric O<sub>2</sub> bands. The O<sub>2</sub> A- and B-band span 7595–7680 Å and 6868–6926 Å respectively.

Table 1 lists the full QPQ9 sample. In Table 2, we first list the sample size, the median  $z_{fg}$ , and the median  $R_{\perp}$  of the quasar pairs that survive the above selection criteria for C II 1334, C IV 1548, and Mg II 2796 respectively. We then provide the summary for the sub-sample with  $z_{fg}$  measured from [O III].

### 3. ANALYSIS

#### 3.1. Stacked Profiles

We create composite spectra that average over the intrinsic scatter in quasar environments, continuum placement errors, and redshift errors. The individual spectra of background quasars are shifted to the rest-frame of the foreground quasars at the transitions of interest. Each spectrum has been linearly interpolated onto a fixed velocity grid centered at  $z_{fg}$  with bins of 100 km s<sup>-1</sup>. For a velocity bin of this size, it is unnecessary to smooth the data to a common spectral resolution. The individual spectra are then combined with a mean or a median statistic. Spectra with broad absorption-line systems and mini-broad absorption-line systems are excluded. Bad pixels in the individual spectra have been masked before generating the composites. Since each quasar pair gives an independent probe of the CGM, each pair has an equal weighting in the stacked profiles, i.e. we do not weight the spectra by the measured S/N near the metal ion transitions. Scatter in the stacked spectra is dominated by randomness in the CGM rather than scatter in the flux of individual observations. The mean statistic of the individual spectra yields a good estimate of the

<sup>5</sup> <https://github.com/specdb/igmspec>

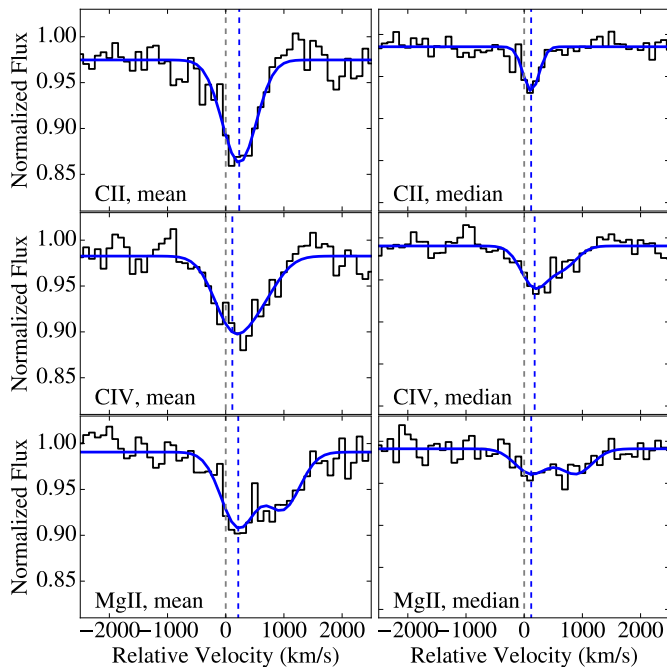


**Figure 2.** Mean and median absorption centered at C II 1334, C IV 1548, and Mg II 2796 of the foreground quasars for all QPQ9 pairs. The composites are shown in thin, black. Overplotted on the composites are Gaussian fits, normalized to pseudo-continua far away from a velocity of  $0 \text{ km s}^{-1}$  relative to  $z_{\text{fg}}$ , and are shown in thick, blue. For the doublets, a second Gaussian with a fixed mean separation and a tied standard deviation is included in the modeling. The absorptions frequently exhibit large velocity widths. The blue dashed lines mark the centroids, which show small positive velocity offsets from  $z_{\text{fg}}$ . The  $1\sigma$  modeling error for the dispersion and the centroid of the C II mean stack are  $27 \text{ km s}^{-1}$  and  $25 \text{ km s}^{-1}$  respectively, which are also the typical modeling errors of the other stacks.

average absorption and preserves equivalent width. The median statistic is less sensitive to outliers. However, the median opacity at any velocity channel is rather small, since the discrete absorbers are spread throughout the entire velocity window. A pixel is not affected unless there are more than 50% of quasar pairs with absorption at its velocity. The analysis on the median velocity field is thus subject to larger uncertainty. In the following we present stacked spectra using both the mean and the median statistic.

In Figure 2, we present mean and median stacks of C II 1334, C IV 1548, and Mg II 2796 absorption of the QPQ9 sample. We focus on the analysis results of the C II mean stack. C IV and Mg II are doublet transitions and it is more challenging to analyze their kinematics. Two results are evident in Figure 2: (i) the mean C II stack exhibits excess absorption spanning a large velocity width; (ii) the mean absorption is likely skewed toward positive velocities.

Visually, there are two absorption components. One component is the uniform depression in the continuum level in the stack resulting from absorbers unassociated with the foreground quasars. The other component comes from absorbers associated with the foreground quasars and distribute around their systemic velocities. To model the absorption, we introduce a Gaussian profile while allowing a constant “pseudo-continuum” to vary.

We perform  $\chi^2$  minimization with each channel given equal weight. From the best-fit to the data, we measure the  $1\sigma$  dispersion of the stack to be  $293 \text{ km s}^{-1}$  and the centroid of the C II stack to be  $+232 \text{ km s}^{-1}$ . The dispersion suggests extreme kinematics, while the centroid suggests an asymmetry that contradicts the standard expectation. The median stack, on the other hand, shows weaker absorption, and the Gaussian model has a more uncertain dispersion and a centroid with smaller offset.

To test whether the dispersion in the average absorption associated with the foreground quasars is well-captured by a Gaussian model, we also calculate the dispersion separately using the standard deviation formula. Specifically, we apply the standard deviation formula to a  $\pm 1300 \text{ km s}^{-1}$  window surrounding the absorption centroid, while fitting a continuum to the rest of the  $\pm 3000 \text{ km s}^{-1}$  window for stacking. The dispersion measured with the above method is essentially the same as that found by fitting a Gaussian. One may also speculate on the existence of a broader absorption component hidden in the depressed continuum. We try replacing the constant absorption component with a broad Gaussian component in our modeling. We find that this second Gaussian component has an amplitude of  $0.030 \pm 0.009$ , i.e. essentially the same amplitude as the initial constant absorption component, and a  $1\sigma$  dispersion of  $3614 \pm 1731 \text{ km s}^{-1}$ , i.e. wider than the entire velocity window for stacking. This weak and very broad component has no effect on the width and the centroid of the narrow, associated Gaussian component. We therefore consider that one single Gaussian component is a good description of the average absorption associated with the foreground quasars. Moreover, narrow associated absorbers of background quasars will not prefer the systemic velocities of the foreground quasars, and hence will not affect the average absorption measured for the foreground quasars. Their contribution to the average absorption should result in a tilt in the pseudo-continuum, which is insignificant.

We also create mean and median stack for the sub-sample with [O III] redshifts and model the absorption with Gaussian best-fit. The C II mean stack for this sub-sample has a dispersion of  $330 \text{ km s}^{-1}$ , and a centroid at  $+235 \text{ km s}^{-1}$ , consistent with the full sample.

To model the mean and median absorption of C IV 1548 and Mg II 1796, we introduce a second Gaussian with separation equal to the doublet separation ( $498 \text{ km s}^{-1}$  and  $769 \text{ km s}^{-1}$  respectively), and tie the dispersion of the two lines in a doublet. We allow the doublet ratio to vary from 2:1 to 1:1. The centroid is degenerate with the doublet ratio in our modeling. This degeneracy is more pronounced for C IV, although we find that a double ratio closer to 2:1 better captures the absorption at the central few pixels. We state that the modeling of the doublets is presented for consistency check, but the analysis focuses on C II. The modeling results show that the velocity fields of C IV and Mg II are consistent with C II, i.e. large dispersion and centroid is skewed toward positive velocities.

The above analyses are summarized in Table 2. The Gaussian models normalized to pseudo-continuum are overplotted on the data stacks in Figure 2.

**Table 2**  
Summary of the Data and Analysis

Measure	C II 1334	C IV 1548	Mg II 2796
For the Full QPQ9 Sample			
Number of pairs	40	110	86
Median $z_{\text{fg}}$	2.04	1.89	1.87
Median $R_{\perp}$	157	191	184
$1\sigma$ dispersion of mean stack ( $\text{km s}^{-1}$ )	$293 \pm 87$	$303 \pm 44$	$295 \pm 200$
Centroid of mean stack ( $\text{km s}^{-1}$ )	$+232 \pm 98$	$+11 \pm 63$	$+215 \pm 124$
Pseudo-continuum of mean stack	0.97	0.98	0.99
$1\sigma$ dispersion of median stack ( $\text{km s}^{-1}$ )	$137 \pm 569$	$218 \pm 71$	$276 \pm 215$
Centroid of median stack ( $\text{km s}^{-1}$ )	$+119 \pm 240$	$+189 \pm 81$	$+121 \pm 201$
Pseudo-continuum of median stack	0.99	0.99	0.99
For the Sub-sample with [OIII] Redshifts			
Number of pairs	15	23	15
Median $z_{\text{fg}}$	2.29	2.29	2.27
Median $R_{\perp}$	183	122	112
$1\sigma$ dispersion of mean stack ( $\text{km s}^{-1}$ )	$330 \pm 103$	$255 \pm 41$	$235 \pm 129$
Centroid of mean stack ( $\text{km s}^{-1}$ )	$+235 \pm 118$	$+130 \pm 77$	$+210 \pm 119$
Pseudo-continuum of mean stack	0.98	0.98	0.95
$1\sigma$ dispersion of median stack ( $\text{km s}^{-1}$ )	$103 \pm 236$	$211 \pm 71$	$175 \pm 114$
Centroid of median stack ( $\text{km s}^{-1}$ )	$+256 \pm 191$	$+210 \pm 111$	$+244 \pm 125$
Pseudo-continuum of median stack	0.99	0.98	0.98

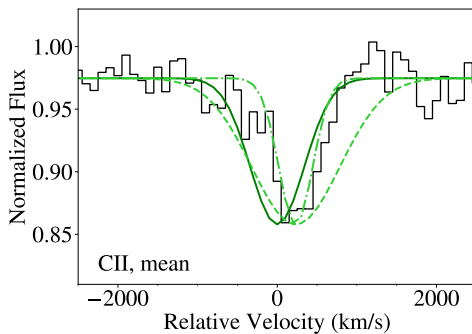


**Figure 3.** The same C II mean stack shown in the first panel of Figure 2 is shown in thin, black. We overplot in dashed, limegreen an absorption profile with  $\sigma_v = 554 \text{ km s}^{-1}$ , which is larger than the observed width by three times the standard deviation in the bootstrap analysis. Motions that produce a velocity width larger than this can be ruled out. We overplot in dot dashed, limegreen an absorption profile with  $\sigma_v = 214 \text{ km s}^{-1}$ , which is smaller than the observed width by three times the modeling error. Unless gravitational and Hubble flows together with redshift error broadening produce a velocity width smaller than this, extra dynamical processes (e.g. outflows) will not be required to explain the observed width. In thick, green, we overplot the Gaussian absorption model of the Monte Carlo simulations generated from a purely clustering argument. The model from clustering analysis is multiplied to the pseudo-continuum level of the stack of the observational data, and broadened by the mean redshift error in the data. While this model has a dispersion within modeling error of the dispersion in the data, the centroid of the stack of the data appears to be redshifted from the systemic. A model with only gravitational motions and Hubble flows cannot explain this putative asymmetry.

### 3.2. Interpretation of the large velocity fields

Under the assumption that the intrinsic dispersion and the redshift uncertainty add in quadrature to give the observed width, we solve for the intrinsic dispersion in the C II mean stack. For the full QPQ9 sample, with the mean  $\sigma_{\text{error}(z)}^{\text{full}} = 189 \text{ km s}^{-1}$ , we recover  $\sigma_{\text{intrinsic}}^{\text{full}} = 224 \text{ km s}^{-1}$ . For the sub-sample with [O III] redshifts, we

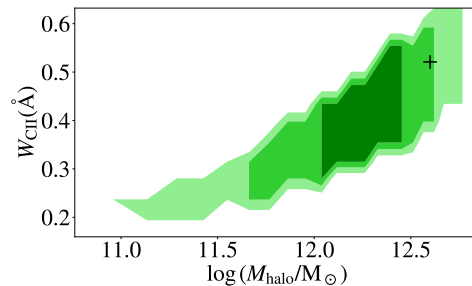


**Figure 4.** Probability distributions of the parameters  $W_{\text{CII}}$  and  $M_{\text{halo}}$ . The plot shows the degeneracy between  $W_{\text{CII}}$  and  $M_{\text{halo}}$  in recovering the intrinsic width of the absorption profile. We mark contours for points that produce an absorption profile of width that is 1, 2, and 3 times the modeling error away from the observed intrinsic width. The intrinsic velocity width corresponding to typical QPQ halo mass is marked with a plus sign, and is contained within the  $2\sigma$  contour.

recover  $\sigma_{\text{intrinsic}}^{[\text{OIII}]} = 323 \text{ km s}^{-1}$ .

To assess the statistical significance of the observed dispersion, we perform a bootstrap analysis by randomly resampling from the full sample 10000 times. We introduce a Gaussian absorption profile to model each bootstrap realization. We find that a width of  $\sigma_v > 554 \text{ km s}^{-1}$  would be larger than the observed by three times the scatter in the bootstrap realizations (overplotted in Figure 3). In other words, taking into account the redshift errors, motions in addition to gravitational and Hubble flows that will produce an intrinsic dispersion  $\sigma_v > 521 \text{ km s}^{-1}$  can be ruled out.

On the contrary,  $\sigma_{\text{rms}} < 70 \text{ km s}^{-1}$  together with Hubble velocities and broadening by redshift errors will result in a velocity width that is more than three times the modeling error away from the observed width (overplotted in Figure 3). This implies that, unless the characteristic  $M_{\text{halo}} < 10^{11.0} M_{\odot}$ , additional dynamical processes are not required to explain the observed width.

Eftekharzadeh et al. (2015) measured the clustering of quasars in the range  $2.2 < z < 2.8$  while Rodríguez-

Torres et al. (2017) measured the clustering of quasars in the range  $1.8 < z < 2.2$ . They estimated that these quasars are hosted by dark matter halos with mass  $M_{\text{halo}} = 10^{12.5} M_{\odot}$  and  $M_{\text{halo}} = 10^{12.6} M_{\odot}$  respectively. If dark matter halos hosting QPQ9 quasars have a characteristic mass  $10^{12.6} M_{\odot}$  and follow an NFW profile (Navarro et al. 1997) with concentration parameter  $c = 4$ , at  $z \approx 2$  the maximum circular velocity is  $345 \text{ km s}^{-1}$ . Tormen et al. (1997) found that the maximum circular velocity is  $\approx 1.4$  times the maximum of the average one-dimensional root-mean-square velocity  $\sigma_{\text{rms}}$ . Hence, the average line-of-sight rms velocity typical of QPQ9 halos is  $\sigma_{\text{rms}} = 246 \text{ km s}^{-1}$ . In QPQ8, we estimated the probability of intercepting a random optically thick absorber is 4%, and clustering would only increase that to 24%. Although motions due to Hubble flows do not dominate, they nevertheless contribute to the observed dispersion. We can investigate whether gravitational motions and Hubble flows are sufficient to reproduce the dispersion in the data, using Monte Carlo methods to simulate the absorption signals.

Since C II systems arise in optically thick absorbers, we may adopt the clustering analysis results of QPQ6. In the absence of clustering, the expected number of absorbers per unit redshift interval for Lyman limit systems, super Lyman limit systems, and damped Ly $\alpha$  systems are respectively  $\ell_{\text{IGM}}^{\text{LLS}}(z) \approx 1.05((1+z)/(1+2.5))^{2.1}$ ,  $\ell_{\text{IGM}}^{\text{SLLS}}(z) \approx 0.44((1+z)/(1+2.5))^{2.1}$ , and  $\ell_{\text{IGM}}^{\text{DLA}}(z) \approx 0.2((1+z)/(1+2.5))^{2.1}$ . The quasar-absorber correlation functions for Lyman limit systems, super Lyman limit systems, and damped Ly $\alpha$  systems are respectively  $\xi_{\text{QA}}^{\text{LLS}}(r) = (r/(12.5 h^{-1} \text{ Mpc}))^{-1.68}$ ,  $\xi_{\text{QA}}^{\text{SLLS}}(r) = (r/(14.0 h^{-1} \text{ Mpc}))^{-1.68}$ , and  $\xi_{\text{QA}}^{\text{DLA}}(r) = (r/(3.9 h^{-1} \text{ Mpc}))^{-1.6}$ . For each quasar pair, we calculate the expected number of optically thick absorbers within  $\pm 3000 \text{ km s}^{-1}$  at a distance  $R_{\perp}$  from the foreground quasar and at  $z_{\text{fg}}$ . Then we generate 1000 mock sightlines. The number of absorbers for each mock spectrum is randomly selected from a Poisson distribution with mean equal to the expected number calculated as above. The absorbers are randomly assigned Hubble velocities, with a probability distribution according to the quasar-absorber correlation functions. The absorbers are randomly assigned additional peculiar velocities drawn from a normal distribution with mean equal to  $0 \text{ km s}^{-1}$  and scatter equal to  $\sigma_{\text{rms}}$ . For each absorber, we assume a rest equivalent width for C II  $W_{\text{CII}}$  and a Gaussian absorption profile. We repeat the above procedure for all 40 quasar pairs, and create a mean stack of the 40000 mock spectra generated. We fit a Gaussian absorption profile multiplied to a constant continuum level to model the stack of mock spectra. We adjust the  $W_{\text{CII}}$  adopted for the absorbers until the amplitude of the best-fit Gaussian of the stack of mock spectra matches the amplitude of the stack of the observational data. We find that  $W_{\text{CII}} \approx 0.5 \text{ \AA}$  well reproduces the amplitude, and the dispersion of the Gaussian absorption model is insensitive to the assumed  $W_{\text{CII}}$  or line profile for one absorber.

In Figure 3, we show a comparison of the observational data stack and the Gaussian absorption model of the Monte Carlo simulations. In the figure, the Gaussian absorption model is broadened by the mean redshift error by adding it in quadrature to the dispersion

in the model. The resulting stack of mock spectra has a  $1\sigma$  dispersion of  $282 \text{ km s}^{-1}$ , about 2 times the modeling error away from the intrinsic dispersion in the C II mean stack for the full sample, and about 2 times the modeling error away from the intrinsic dispersion in the stack of the sub-sample with [O III] redshifts as well. One may also consider whether absorbers in Hubble flow and cosmological distances show peculiar velocities that are typical for quasar-mass halos, and adopt a different  $\sigma_{\text{rms}}$  accordingly. The best-studied coeval, more typical star-forming galaxies are the Lyman-break galaxies. Their clustering strength implies a characteristic halo mass of  $M_{\text{halo}} \approx 10^{11.6} M/M_{\odot}$  (Bielby et al. 2013; Malkan et al. 2017), corresponding to  $\sigma_{\text{rms}} = 114 \text{ km s}^{-1}$ . If we adopt this smaller  $\sigma_{\text{rms}}$  instead, for absorbers outside the loosely defined quasar CGM boundary, at  $\gtrsim 300 \text{ kpc}$ , the stack of mock spectra will have a  $1\sigma$  dispersion of  $247 \text{ km s}^{-1}$ . This is again within modeling errors of the observed intrinsic dispersion. We also test for the sensitivity of this measured dispersion to the correlation functions adopted. The QPQ6 clustering analysis is performed on only the strongest absorber near  $z_{\text{fg}}$ , and a low  $R_{\perp}$  sightline may in fact intercept more than one optically thick absorber. We double the number of absorbers for each mock sightline, and find the measured dispersion only increases by several  $\text{km s}^{-1}$ . Thus, before the putative asymmetry is confirmed, the hypothesis that the observed velocity width is only produced by a combination of gravitational motions and Hubble flows cannot be ruled out. Extra dynamical processes are not necessary to explain the large velocity fields.

Although we acknowledge the possibility that our Gaussian model does not capture all the powers at extreme velocities, we also caution that occasional large kinematic offsets do not make a strong case against gravitational motions. Firstly, quasars occasionally inhabit extremely overdense environments such as protoclusters (e.g., Hennawi et al. 2015). Secondly, the probability of intercepting a random, unassociated absorber is boosted by large-scale clustering. Hence occasional extreme velocities would not necessitate outflows. Our preferred kinematic measure is thus the dispersion in the average absorption.

In Figure 4, We show the probability distributions of the degenerate parameters  $W_{\text{CII}}$  and  $M_{\text{halo}}$  in recovering the intrinsic width of the absorption profile. We require that the amplitude of the absorption is reproduced within 3 times its modeling error, and mark contours for points in  $(W_{\text{CII}}, M_{\text{halo}})$ -space that produce an absorption profile of width within 1, 2, and 3 times the modeling error of the observed intrinsic width. From the figure, a higher  $W_{\text{CII}}$  means the  $M_{\text{halo}}$  that will reproduce the observed width is higher. If there are no extra dynamical processes, the intrinsic velocity width corresponding to typical QPQ halo mass is contained within the  $2\sigma$  contour.

### 3.3. Interpretation of the asymmetric absorption

We quote the standard deviation in the bootstrap realizations to be the scatter in the centroids of the data. The scatters  $\approx 100 \text{ km s}^{-1}$  are comparable to the measured offsets, indicating large intrinsic variation in quasar CGM environments (see also QPQ8). In Figure 5, we show the distribution of the absorption centroids from bootstrapping on the C II mean stack. We find that



97% of the centroids are at positive velocities. We place a generous  $3\sigma$  upper limit to the small offset of the centroid from  $z_{\text{fg}}$  for the C II mean absorption at  $\delta v < +526 \text{ km s}^{-1}$ . Given the large intrinsic scatter, we do not attempt to explore whether there exists relative asymmetry among the C II, C IV, and Mg II absorption.

One may ask whether absorption from C II\* 1335 may bias the measurement of the C II 1334 velocity centroid. In the stacks at C II 1334, absorption from C II\* 1335 would manifest as a component redshifted by  $+264 \text{ km s}^{-1}$ . In the higher resolution data from QPQ8, we identify nine C II-bearing subsystems where absorption from C II\* 1335 is not blended with C II 1334. Their mean C II to C II\* equivalent width ratio is 0.2. Among these nine subsystems, only one, labeled J1420+1603F in QPQ8, has a C II\* 1335 equivalent width comparable to C II 1334. We simulate that absorption from C II\* may only bias the C II centroid by  $\approx +40 \text{ km s}^{-1}$ . Hence, contamination from C II\* 1335 could not be responsible for the observed redshift in the centroid.

One may also ask whether the measured positive offsets come from systematic bias in redshift measurements due to the Baldwin effect (Baldwin 1977). Shen et al. (2016b) reported that, the [O III] emission of  $z \sim 2$  quasars is more asymmetric and weaker than that in typically less luminous low- $z$  quasars. To test for this potential source of bias, we create another mean stack at C II 1334 by replacing the [O III] redshifts by a redshift measured from the more symmetric Mg II or H $\alpha$  emission when available. We are able to replace for 11 out of the 15 systems with [O III] redshifts in the original sample. The new stack is similar in velocity structure and again shows a positive offset  $\approx +303 \text{ km s}^{-1}$ . We thus conclude that our algorithm for measuring redshifts is not severely biased by the blue wing of the [O III] emission-line.

Motivated by the study of Mg II absorbers surrounding  $z \sim 1$  quasars by Johnson et al. (2015), we also generate a mean-stacked spectrum for Mg II 2796 for lower redshift quasar pairs. We select quasars with  $0.4 < z_{\text{fg}} < 1.6$  and use the same other selection criteria as the main QPQ9 sample. The quasar pairs are selected from the igmspec database, with  $z_{\text{fg}}$  measured by Hewett & Wild (2010). For quasars with  $z_{\text{fg}} < 0.84$ , as redshift determination is dominated by [O III] emission, a shift of  $+48 \text{ km s}^{-1}$  is applied to bring the emission-line redshift to the systemic. For quasars with  $0.84 < z_{\text{fg}} < 1.6$ , as redshift determination is dominated by Mg II emission, a shift of  $+57 \text{ km s}^{-1}$  is applied. There are 233 pairs selected, with a median  $z_{\text{fg}}$  of 0.90 and a median  $R_{\perp}$  of 208 kpc. We present the mean stack in Figure 6. The absorption is weaker than the  $z \sim 2$  main QPQ9 sample. Gaussian absorption models fitted to the stack recover a centroid of  $-11 \pm 379 \text{ km s}^{-1}$  and a dispersion of  $172 \text{ km s}^{-1}$ . The average offset from  $0 \text{ km s}^{-1}$  is much smaller than the offsets in the  $z \sim 2$  sample.

Since the large scatter in the centroids represents intrinsic variation rather than redshift errors, and the Mg II stack for lower redshift suggests a different centroid, we consider that systematic biases are unlikely to explain the asymmetry signal in the  $z \sim 2$  sample. In the Discussion section, we discuss two possible explanations for the asymmetry.

#### 4. DISCUSSION

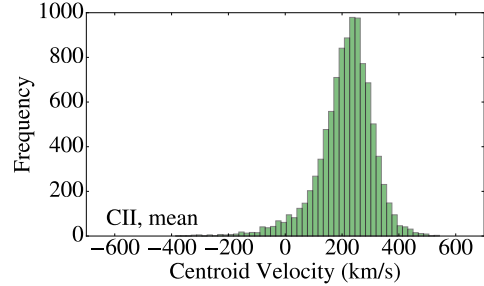


**Figure 5.** Histogram of the absorption centroids of 10000 bootstrap realizations of the data sample for the C II mean stack. 97% of the centroids are positively offset from  $z_{\text{fg}}$ .

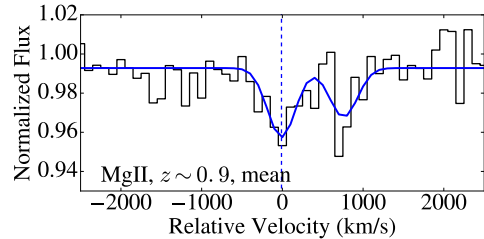


**Figure 6.** Mean stack at Mg II 2796, for a lower redshift sample of quasar pairs at  $z \sim 0.9$ . Line-style coding is the same as in Figure 2. The centroid is approximately at  $0 \text{ km s}^{-1}$ , and the absorption is weaker than the main QPQ9 sample.

At low redshift, both symmetric and asymmetric ionization cones around quasars and AGNs are observed. In the extended emission-line region of 4C37.43, most of the [O III] emission is blueshifted (Fu & Stockton 2007), but there are counter examples in less extended sources in Fu & Stockton (2009). Recently, there has been Fabry-Perot interferometric data for less extended narrow-line regions in more nearby sources (Keel et al. 2015, 2017), which show mostly symmetric velocity fields and gas distributions.

In the following, we explore two possible explanations for the non-dynamical processes that provides the putative asymmetry. The explanations arise from a transverse proximity effect (QPQ4), which is the suppression of opacity in background sightlines passing close to foreground quasars.

One possibility is an asymmetric radiation field that preferentially ionizes the gas moving toward the observer, where the quasar is known to shine. Alternatively, the asymmetric radiation field may preferentially ionizes the gas at smaller Hubble velocity than the quasar. In Figure 7, we show a cartoon of a quasar that is blocked in the direction pointing away from the observer. The gas observed in absorption preferentially lies behind the quasar. Roos et al. (2015) and Gabor & Bournaud (2014) performed simulations of a high-redshift disk galaxy including thermal AGN feedback and calculated radiative transfer in post-processing. They found the ionization radiation is typically asymmetric, due to either a dense clump that lies on one edge of the black hole or the black hole's location being slightly above the disk. Faucher-Giguère et al. (2016) represents the only simulation so far that is able to reproduce the substantial amount of cool gas in quasar-mass haloes. We eagerly await their group to compare the fraction of gas in inflows and outflows.

FIG. 7 A cartoon showing a unipolar quasar. The gas observed in low- to intermediate-ion absorption preferentially lies behind the quasar, and is shadowed from the ionizing radiation.

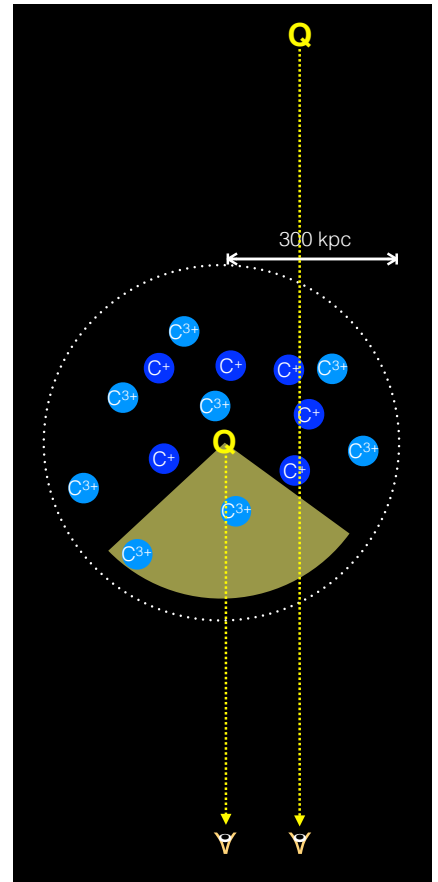
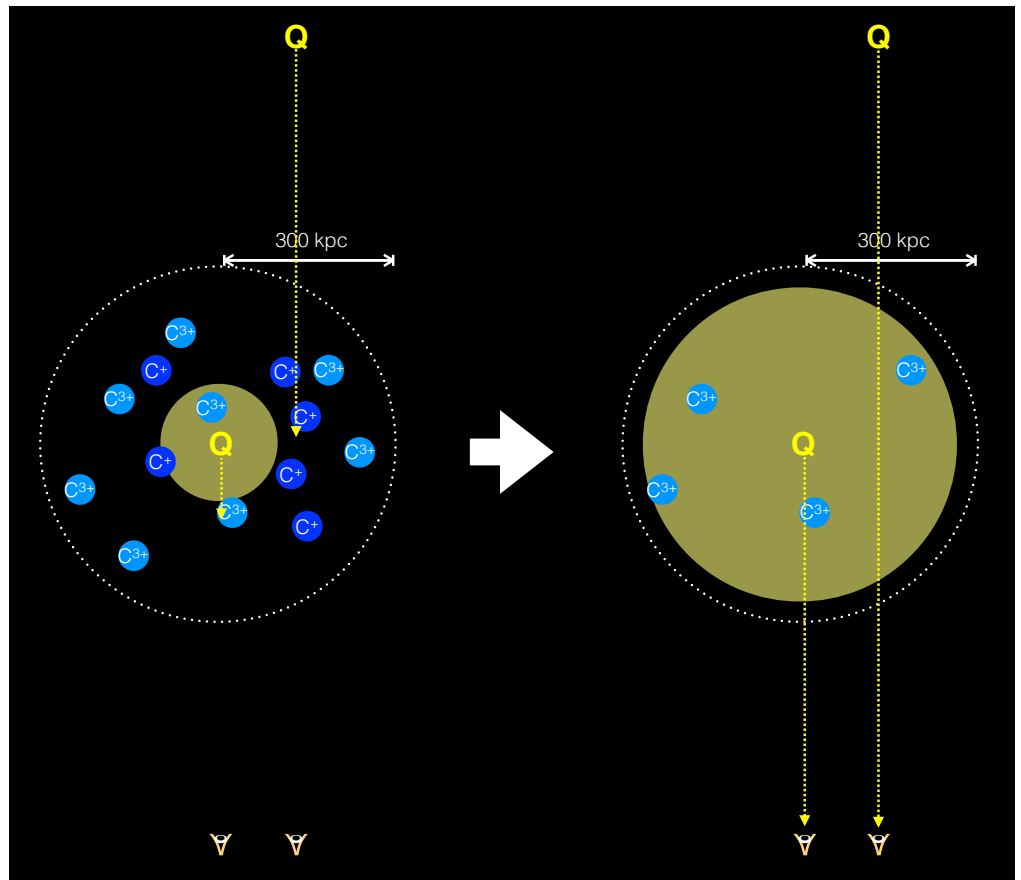


FIG. 8 A cartoon showing the finite lifetime of quasar episodes as an explanation to the asymmetric absorption. The setup on the left shows that the foreground quasar has not been shining long enough for its ionizing radiation to reach the gas behind it, when the light from the background quasar reaches. The setup on the right shows the scenario after an amount of time comparable to the light travelling time across CGM scale. Gas in front of the foreground quasar has been ionized, by the time the light from the background quasar reaches.



Another possible explanation arises from the finite lifetime of quasar episodes. Figure 8 presents a cartoon for a light travel time argument. The light from the background quasar may arrive at the gas behind the foreground quasar before the ionizing radiation from the foreground quasar arrives.

The first explanation above to asymmetric absorption requires that the quasars emit their ionizing radiation anisotropically, while the second explanation requires the quasars emit their ionizing radiation intermittently. Both explanations will require the line-of-sight motions of the gas to be not in a net inflow. Were the gas flowing into the galaxy instead, the velocity centroid would be negative. Under both scenarios, low ions should be redshifted while high ions should be blueshifted. Using Cloud photoionization models, we find that, for the typical quasar luminosity of our sample, a CGM gas that is directly illuminated is highly ionized and shows only marginally detectable C IV absorption. The redshifted C IV may be regarded as an intermediate ion, and a blueshifted absorption signal needs to be searched in a higher ion.

We test the case of Hubble flows versus galactic-scale outflows in producing the putative asymmetry. Anisotropic emission is degenerate with intermittent emission in their asymmetric light-echo in the observer’s frame. We first consider the scenario where the quasar’s lifetime is infinite, and the observed asymmetric absorption is only produced by anisotropic emission. We try implementing an arbitrary quasar opening angle in our Monte Carlo simulations to reproduce an absorption centroid that is redshifted from the systemic. In QPQ6, we argued that the observed anisotropic clustering of optically thick systems around quasars demands that a quasar’s radiation field must affect optically thick systems on Mpc scales. Hence in this test, we set the incidence of absorbers happening within the quasar opening angle to be zero, for absorbers at all distances from the quasar. In the case without outflows, even if we set the opening angle to be  $180^\circ$ , i.e. absorption only happens at positive velocities, the mean absorption centroid would merely reach  $\approx +85 \text{ km s}^{-1}$ . Hence, the observed  $\delta v \approx +200 \text{ km s}^{-1}$  shift in the mean absorption cannot be produced by asymmetric distribution in Hubble velocities alone. This suggests the presence of an outflow component to account for extra asymmetry in line-of-sight velocities. In order to produce the observed intrinsic dispersion and centroid of the mean absorption by C II, we must add a radial outflow speed of  $\approx 450 \text{ km s}^{-1}$  to the absorbers and a unipolar quasar opening angle of  $\approx 180^\circ$ . Next, we consider another scenario where the quasar is isotropic, and the asymmetric absorption is only produced by short episodic lifetime. We further make the assumption the luminosity is constant during a quasar episode. In the quasar’s rest frame, the light echo would be observed as a spherical region with the quasar

at the origin. In the observer’s frame, due to finite light travel time, the light-echo would not be spherically symmetric. The light-echo from the quasar at its luminosity  $t$  yr earlier traces a paraboloid with the quasar at the focus and the vertex  $t/2$  ly behind it (Adelberger 2004; Visbal & Croft 2008). We find that, to reproduce the observation, the CGM absorbers need to have a radial outflow speed  $\approx 420 \text{ km s}^{-1}$  and the quasar must have shined for  $\approx 0.4 \times 10^6$  yr. For the anisotropy-only scenario, the opening angle deduced is rather large compared to literature findings, which give  $30^\circ$ – $90^\circ$  (e.g., Trainor & Steidel 2013; Borisova et al. 2016). For the intermittence-only scenario, if the quasars are on averaged observed near the middle of the episode, the lifetime deduced is somewhat small compared to other existing constraints from observations and simulations, which give  $10^6$ – $10^8$  yr (e.g., Martini 2004; Hopkins et al. 2005). We thus speculate that the asymmetric absorption is the result of a combination of anisotropic and intermittent emission.

We note that, Turner et al. (2017) conclude that the clustering of low to intermediate ions around Lyman-break galaxies in velocity space is most consistent with gas that is inflowing on average. The different conclusion from our analysis may originate from the higher masses of our systems, the presence of quasar-driven outflows (e.g., Greene et al. 2012), and/or starburst-driven outflows that are correlated with the presence of quasars (e.g., Barthel et al. 2017).

Motivated by the asymmetry found in metal ion absorption in the CGM using precise  $z_{\text{fg}}$  measurements, and the asymmetry found by Kirkman & Tytler (2008) in H I on larger scales, we are assembling a sample of quasar pairs with precise  $z_{\text{fg}}$  measurements to study this asymmetry in H I (J. F. Hennawi et al. 2018, in preparation). In conclusion, we observe large and positively skewed velocity fields in absorption, of metal ions in the CGM of  $z \sim 2$  massive galaxies hosting quasars. We argue that, the observation of large velocity fields alone can be accounted for by gravitational motions and Hubble flows and does not necessitate outflows. However, we argue that the positive skew suggests the detected gas is in outflow on average, and the quasars shine preferentially toward the observer and/or intermittently.

MWL is immensely grateful to the referee’s constructive comments, which help strengthen the paper. JXP and MWL acknowledge support from the National Science Foundation (NSF) grants AST-1010004 and AST-1412981. The authors gratefully acknowledge the support which enabled these observations at the Keck, Gemini, Large Binocular Telescope, Very Large Telescope, Las Campanas, and Palomar Observatories. The authors acknowledge the sharing of private data by Yue Shen. MWL thanks Hai Fu for a discussion on extended emission-line regions, T.-K. Chan for a discussion on CGM simulations, and Chi Po Choi and Yat Tin Chow for discussions on statistics.

## APPENDIX

### LINE-OF-SIGHT ABSORPTION

In the previous QPQ papers, we argued that optically thick absorbers in the vicinity of quasars are distributed anisotropically. We now have the means to show this anisotropic clustering explicitly. Given that the techniques for

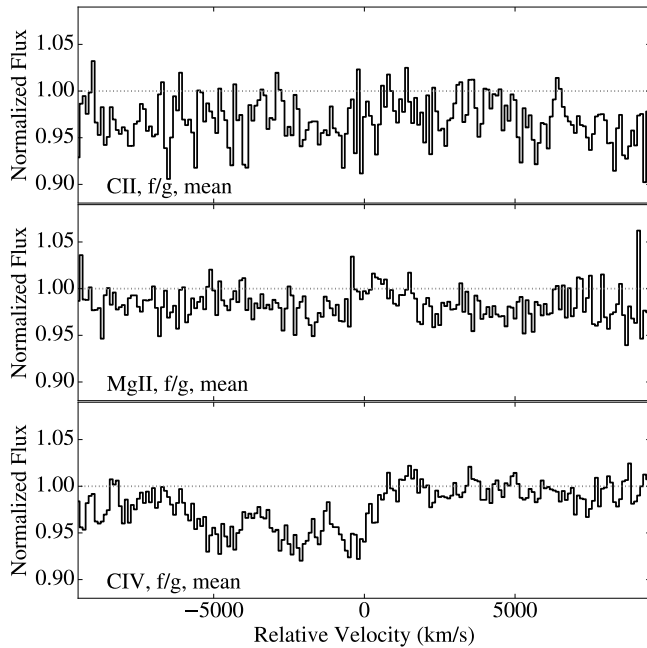


**Figure 9.** Mean stacks of the foreground quasar spectra at C II 1334, C IV 1548, and Mg II 2796 for the QPQ9 sample. For C II and Mg II, the mean absorption is weaker than that in the background stacks, and there is no evidence for an excess at  $z_{fg}$ . The stack for C IV, which includes line-of-sight absorbers at all distances, shows a large, blueshifted mean velocity field.

stacking spectra are established, it is straightforward to apply the same techniques to stack the foreground quasar spectra. In Figure 9, we present mean stacks of foreground quasar spectra for the QPQ9 sample. We require that the spectra survive a S/N cut of 5.5 per rest-frame Å at C II 1334, C IV 1548, or Mg II 2796 at  $z_{fg}$ . In contrast to the large equivalent widths exhibited in the stacks of background spectra, C II and Mg II mean absorption along the line-of-sight to the foreground quasars is weaker, and an excess at  $z_{fg}$  is absent. This supports a scenario where the ionizing radiation of the foreground quasars are anisotropic and/or intermittent. For C IV 1548, this stack of all line-of-sight absorbers, which include absorbers intrinsic to and far away from the quasar, shows a large, blueshifted velocity field. This excess C IV absorption has been well studied as narrow associated absorption line systems (e.g., Wild et al. 2008). We note that, in the  $z \sim 4$  sample of narrow associated absorbers analyzed by Perrotta et al. (2016) and Perrotta et al. (2018, in preparation), a higher ionization state is similarly found along the line-of-sight to quasars compared to across the line-of-sight. In particular, an excess of N V absorption is found in proximity to the host quasars.

## REFERENCES

- Adelberger, K. L. 2004, *ApJ*, 612, 706  
 Baldwin, J. A. 1977, *ApJ*, 214, 679  
 Barthel, P., Podigachoski, P., Wilkes, B., & Haas, M. 2017, *ApJ*, 843, L16  
 Bielby, R., Hill, M. D., Shanks, T., Crighton, N. H. M., Infante, L., Bornancini, C. G., Francke, H., Héraudeau, P., Lambas, D. G., Metcalfe, N., Minniti, D., Padilla, N., Theuns, T., Tummuangpak, P., & Weilbacher, P. 2013, *MNRAS*, 430, 425  
 Bergeron, J., & Boisse, P. 1991, *Advances in Space Research*, 11, 241  
 Borisova, E., Lilly, S. J., Cantalupo, S., Prochaska, J. X., Rakic, O., & Worseck, G. 2016, *ApJ*, 830, 120  
 Boroson, T. 2005, *AJ*, 130, 381  
 Cantalupo, S., Arrigoni-Battaia, F., Prochaska, J. X., Hennawi, J. F., & Madau, P. 2014, *Nature*, 506, 63  
 Churchill, C. W., Kacprzak, G. G., Steidel, C. C., Spitler, L. R., Holtzman, J., Nielsen, N. M., & Trujillo-Gomez, S. 2012, *ApJ*, 760, 68  
 Eftekharzadeh, S., Myers, A. D., White, M., Weinberg, D. H., Schneider, D. P., Shen, Y., Font-Ribera, A., Ross, N. P., Paris, I., & Streblyanska, A. 2015, *MNRAS*, 453, 2779  
 Faucher-Giguère, C.-A., Feldmann, R., Quataert, E., Kereš, D., Hopkins, P. F., & Murray, N. 2016, *MNRAS*, 461, L32  
 Fu, H., & Stockton, A. 2007, *ApJ*, 666, 794  
 —. 2009, *ApJ*, 690, 953  
 Fumagalli, M., Prochaska, J. X., Kasen, D., Dekel, A., Ceverino, D., & Primack, J. R. 2011, *MNRAS*, 418, 1796  
 Gabor, J. M., & Bournaud, F. 2014, *MNRAS*, 441, 1615  
 Gauthier, J.-R. 2013, *MNRAS*, 432, 1444  
 Greene, J. E., Zakamska, N. L., & Smith, P. S. 2012, *ApJ*, 746, 86  
 Hennawi, J. F., Prochaska, J. X., Burles, S., Strauss, M. A., Richards, G. T., Schlegel, D. J., Fan, X., Schneider, D. P., Zakamska, N. L., Oguri, M., Gunn, J. E., Lupton, R. H., & Brinkmann, J. 2006, *ApJ*, 651, 61  
 Hennawi, J. F., Prochaska, J. X., Cantalupo, S., & Arrigoni-Battaia, F. 2015, *Science*, 348, 779  
 Hewett, P. C., & Wild, V. 2010, *MNRAS*, 405, 2302  
 Ho, S. H., Martin, C. L., Kacprzak, G. G., & Churchill, C. W. 2017, *ApJ*, 835, 267  
 Hopkins, P. F., Hernquist, L., Martini, P., Cox, T. J., Robertson, B., Di Matteo, T., & Springel, V. 2005, *ApJ*, 625, L71  
 Johnson, S. D., Chen, H.-W., & Mulchaey, J. S. 2015, *MNRAS*, 452, 2553  
 Keel, W. C., Lintott, C. J., Maksym, W. P., Bennert, V. N., Chojnowski, S. D., Moiseev, A., Smirnova, A., Schawinski, K., Sartori, L. F., Urry, C. M., Pancoast, A., Schirmer, M., Scott, B., Showley, C., & Flatland, K. 2017, *ApJ*, 835, 256  
 Keel, W. C., Maksym, W. P., Bennert, V. N., Lintott, C. J., Chojnowski, S. D., Moiseev, A., Smirnova, A., Schawinski, K., Urry, C. M., Evans, D. A., Pancoast, A., Scott, B., Showley, C., & Flatland, K. 2015, *AJ*, 149, 155  
 Kereš, D., Katz, N., Fardal, M., Davé, R., & Weinberg, D. H. 2009, *MNRAS*, 395, 160  
 Kirkman, D., & Tytler, D. 2008, *MNRAS*, 391, 1457  
 Lau, M. W., Prochaska, J. X., & Hennawi, J. F. 2016, *ApJS*, 226, 25

- Malkan, M. A., Cohen, D. P., Maruyama, M., Kashikawa, N., Ly, C., Ishikawa, S., Shimasaku, K., Hayashi, M., & Motohara, K. 2017, *ApJ*, 850, 5
- Martin, C. L. 2005, *ApJ*, 621, 227
- Martini, P. 2004, *Coevolution of Black Holes and Galaxies*, 169
- Muzahid, S., Kacprzak, G. G., Churchill, C. W., Charlton, J. C., Nielsen, N. M., Mathes, N. L., & Trujillo-Gomez, S. 2015, *ApJ*, 811, 132
- Navarro, J. F., Frenk, C. S., & White, S. D. M. 1997, *ApJ*, 490, 493
- Pâris, I., Petitjean, P., Ross, N. P., Myers, A. D., Aubourg, É., Streblyanska, A., Bailey, S., Armengaud, É., Palanque-Delabrouille, N., Yèche, C., Hamann, F., Strauss, M. A., Albareti, F. D., Bovy, J., Bizyaev, D., Niel Brandt, W., Brusa, M., Buchner, J., Comparat, J., Croft, R. A. C., Dwelly, T., Fan, X., Font-Ribera, A., Ge, J., Georgakakis, A., Hall, P. B., Jiang, L., Kinemuchi, K., Malanushenko, E., Malanushenko, V., McMahon, R. G., Menzel, M.-L., Merloni, A., Nandra, K., Noterdaeme, P., Oravetz, D., Pan, K., Pieri, M. M., Prada, F., Salvato, M., Schlegel, D. J., Schneider, D. P., Simmons, A., Viel, M., Weinberg, D. H., & Zhu, L. 2017, *A&A*, 597, A79
- Perrotta, S., D'Odorico, V., Prochaska, J. X., Cristiani, S., Cupani, G., Ellison, S., López, S., Becker, G. D., Berg, T. A. M., Christensen, L., Denney, K. D., Hamann, F., Pâris, I., Vestergaard, M., & Worseck, G. 2016, *MNRAS*, 462, 3285
- Prochaska, J. X. 2017, *Astronomy and Computing*, 19, 27
- Prochaska, J. X., Hennawi, J. F., Lee, K.-G., Cantalupo, S., Bovy, J., Djorgovski, S. G., Ellison, S. L., Lau, M. W., Martin, C. L., Myers, A., Rubin, K. H. R., & Simcoe, R. A. 2013a, *ApJ*, 776, 136
- Prochaska, J. X., Hennawi, J. F., & Simcoe, R. A. 2013b, *ApJ*, 762, L19
- Prochaska, J. X., Lau, M. W., & Hennawi, J. F. 2014, *ApJ*, 796, 140
- Prochaska, J. X., Weiner, B., Chen, H.-W., Mulchaey, J., & Cooksey, K. 2011, *ApJ*, 740, 91
- Rakic, O., Schaye, J., Steidel, C. C., & Rudie, G. C. 2012, *ApJ*, 751, 94
- Richards, G. T., Vanden Berk, D. E., Reichard, T. A., Hall, P. B., Schneider, D. P., SubbaRao, M., Thakar, A. R., & York, D. G. 2002, *AJ*, 124, 1
- Rodríguez-Torres, S. A., Comparat, J., Prada, F., Yepes, G., Burtin, E., Zarrouk, P., Laurent, P., Hahn, C., Behroozi, P., Klypin, A., Ross, A., Tojeiro, R., & Zhao, G.-B. 2017, *MNRAS*, 468, 728
- Roos, O., Juneau, S., Bournaud, F., & Gabor, J. M. 2015, *ApJ*, 800, 19
- Rubin, K. H. R., Prochaska, J. X., Koo, D. C., Phillips, A. C., Martin, C. L., & Winstrom, L. O. 2014, *ApJ*, 794, 156
- Rudie, G. C., Newman, A. B., & Murphy, M. T. 2017, *ApJ*, 843, 98
- Rupke, D. S., Veilleux, S., & Sanders, D. B. 2005, *ApJS*, 160, 115
- Schneider, D. P., Richards, G. T., Hall, P. B., Strauss, M. A., Anderson, S. F., Boroson, T. A., Ross, N. P., Shen, Y., Brandt, W. N., Fan, X., Inada, N., Jester, S., Knapp, G. R., Krawczyk, C. M., Thakar, A. R., Vanden Berk, D. E., Voges, W., Yanny, B., York, D. G., Bahcall, N. A., Bizyaev, D., Blanton, M. R., Brewington, H., Brinkmann, J., Eisenstein, D., Frieman, J. A., Fukugita, M., Gray, J., Gunn, J. E., Hiben, P., Ivezić, Ž., Kent, S. M., Kron, R. G., Lee, M. G., Lupton, R. H., Malanushenko, E., Malanushenko, V., Oravetz, D., Pan, K., Pier, J. R., Price, III, T. N., Saxe, D. H., Schlegel, D. J., Simmons, A., Snedden, S. A., SubbaRao, M. U., Szalay, A. S., & Weinberg, D. H. 2010, *AJ*, 139, 2360
- Shen, Y., Brandt, W. N., Richards, G. T., Denney, K. D., Greene, J. E., Grier, C. J., Ho, L. C., Peterson, B. M., Petitjean, P., Schneider, D. P., Tao, C., & Trump, J. R. 2016a, *ApJ*, 831, 7
- Shen, Y., Horne, K., Grier, C. J., Peterson, B. M., Denney, K. D., Trump, J. R., Sun, M., Brandt, W. N., Kochanek, C. S., Dawson, K. S., Green, P. J., Greene, J. E., Hall, P. B., Ho, L. C., Jiang, L., Kinemuchi, K., McGreer, I. D., Petitjean, P., Richards, G. T., Schneider, D. P., Strauss, M. A., Tao, C., Wood-Vasey, W. M., Zu, Y., Pan, K., Bizyaev, D., Ge, J., Oravetz, D., & Simmons, A. 2016b, *ApJ*, 818, 30
- Shen, Y., Richards, G. T., Strauss, M. A., Hall, P. B., Schneider, D. P., Snedden, S., Bizyaev, D., Brewington, H., Malanushenko, V., Malanushenko, E., Oravetz, D., Pan, K., & Simmons, A. 2011, *ApJS*, 194, 45
- Somerville, R. S., & Davé, R. 2015, *ARA&A*, 53, 51
- Steidel, C. C., Erb, D. K., Shapley, A. E., Pettini, M., Reddy, N., Bogosavljević, M., Rudie, G. C., & Rakic, O. 2010, *ApJ*, 717, 289
- Tormen, G., Bouchet, F. R., & White, S. D. M. 1997, *MNRAS*, 286, 865
- Trainor, R., & Steidel, C. C. 2013, *ApJ*, 775, L3
- Tripp, T. M., Meiring, J. D., Prochaska, J. X., Willmer, C. N. A., Howk, J. C., Werk, J. K., Jenkins, E. B., Bowen, D. V., Lehner, N., Sembach, K. R., Thom, C., & Tumlinson, J. 2011, *Science*, 334, 952
- Tumlinson, J., Thom, C., Werk, J. K., Prochaska, J. X., Tripp, T. M., Katz, N., Davé, R., Oppenheimer, B. D., Meiring, J. D., Ford, A. B., O'Meara, J. M., Peebles, M. S., Sembach, K. R., & Weinberg, D. H. 2013, *ApJ*, 777, 59
- Turner, M. L., Schaye, J., Crain, R. A., Rudie, G., Steidel, C. C., Strom, A., & Theuns, T. 2017, *MNRAS*, 471, 690
- Visbal, E., & Croft, R. A. C. 2008, *ApJ*, 674, 660
- Weiner, B. J., Coil, A. L., Prochaska, J. X., Newman, J. A., Cooper, M. C., Bundy, K., Conselice, C. J., Dutton, A. A., Faber, S. M., Koo, D. C., Lotz, J. M., Rieke, G. H., & Rubin, K. H. R. 2009, *ApJ*, 692, 187
- Wild, V., Kauffmann, G., White, S., York, D., Lehnert, M., Heckman, T., Hall, P. B., Khare, P., Lundgren, B., Schneider, D. P., & vanden Berk, D. 2008, *MNRAS*, 388, 227
- Zahedy, F. S., Chen, H.-W., Rauch, M., Wilson, M. L., & Zabludoff, A. 2016, *MNRAS*, 458, 2423